BNL-229392-2026-JAAM

Dual aggregation steering in bulk-heterojunction via solvent engineering toward efficient and stable binary organic solar cells

Y. Lin, R. Li

To be published in "Chemical Engineering Journal"

January 2026

Photon Sciences

Brookhaven National Laboratory

U.S. Department of Energy

USDOE Office of Science (SC), Basic Energy Sciences (BES). Scientific User Facilities (SUF)

DISCLAIMER

Dual Aggregation Steering in Bulk-Heterojunction via Solvent Engineering Towards Efficient and Stable Binary Organic Solar Cells

Yijing Lin,[a] Bing Zheng,[b*] Xingting Liu,[a] Huizhen Xu,[a] Liyang Yu,[c*] Ruipeng Li,[d] Xin Song,[a*] Weiguo Zhu[a*]

a: School of Materials Science and Engineering, Jiangsu Engineering Research Center of Light-Electricity-Heat Energy-Converting Materials and Applications, Jiangsu Collaborative Innovation Center of Photovoltaic Science and Engineering, Changzhou University, Changzhou, 213164, P.R. China.

E-mail: xin.song@cczu.edu.cn,zhuwg18@126.com

b: School of pharmacy, Shandong Second Medical University, Weifang, Shandong, 261053, P. R. China.

E-mail: zhengbing@sdsmu.edu.cn

c: Research Institute of Frontier Science, Southwest Jiaotong University, Chengdu 610031, P. R. China

E-mail: liyangyu@swjtu.edu.cn

d: National Synchrotron Light Source (NSLS II), Brookhaven National Laboratory, Upton, NY, 11973

Keywords:

Organic solar cells

Morphology control

Mixed solvent processing

H/J-aggregation

Abstract: In high-performance organic solar cells (OSCs), efficient charge transport hinges on a well-optimized morphology of the photoactive layer, which depends critically on controlled aggregation and favorable interactions between donor and acceptor materials. In this work, we introduce a cascade solvent system comprising high-boiling-point ethylbenzene (EB) and low-boiling-point chloroform (CF) to finely tune the aggregation behavior of the D18 donor and L8-BO acceptor. The incorporation of EB not only promotes the H-aggregation of D18 and the J-aggregation of L8-BO but also facilitates the formation of ideal nanoscale phase separation, thereby suppressing bimolecular recombination. As a result, devices processed with the EB/CF solvent blend achieve a best power conversion efficiency (PCE) of 19.6% and enhanced operational stability, outperforming those fabricated with pure CF (17.1%). This study offers a reliable and effective strategy for optimizing donor and acceptor aggregation, providing a viable pathway toward higher-performance OSCs.

1. Introduction

Organic solar cells (OSCs) have gained significant attention owing to their notable advantages, including flexibility, light weight, and suitability for large-area fabrication[1-3]. Recent progress in the development of organic photovoltaic materials has led to remarkable improvements in charge transport properties, with state-of-the-art OSCs now achieving power conversion efficiencies (PCEs) beyond 20%[4, 5]. This rapid advancement has been fueled by parallel innovations in multiple fronts, including the development of novel device architectures such as layered all-polymer cells and layer-by-layer processing[6, 7], as well as the incorporation of new functional materials to manage energy loss[8]. A key factor driving this progress is the recognized importance of molecular aggregation in governing charge transfer processes, which has stimulated extensive efforts to precisely control molecular assembly and packing behavior[9, 10].

It is well established that the molecular packing arrangements in organic photovoltaic materials are key factors in regulating charge transport efficiency[11, 12]. Generally, the aggregation of organic photovoltaic materials can be categorized into H- and J-type modes, distinguished by their distinct molecular packing geometries and electronic coupling characteristics[13, 14]. H-aggregates typically form through head-to-head π-stacking with dominant interchain coupling, whereas J-aggregates adopt a head-to-tail arrangement favoring intrachain interactions[15-17]. Spectroscopic and computational studies further suggest that hole transport correlates strongly with interchain coupling in H-aggregates, while electron relaxation processes exhibit greater dependence on the intrachain character of J-aggregates[18]. Therefore, J-aggregation is typically associated with enhanced molecular planarity and favored intramolecular electron transport, whereas H-aggregation facilitates coplanar stacking and promotes intermolecular hole transport[19, 20]. This distinction suggests that rational control over molecular aggregation can effectively modulate charge transport pathways, offering a viable strategy for the simultaneous enhancement of both electron and hole mobility[21-23]. This perspective outlines a fundamental design strategy in which H-

aggregation is promoted in the donor to enhance hole transport while J-aggregation is steered in the acceptor to improve electron transport. Within this framework, the deliberate control of aggregation type and extent becomes essential, which can offer a clear route to optimized device performance[24-26].

Here, we developed a solvent strategy using a mixture of ethylbenzene (EB) and chloroform (CF) to promote H-aggregation in the D18 donor and J-aggregation in the L8-BO acceptor. Compared to films processed with pure CF, those fabricated with the EB/CF blend showed distinct blue- and red-shifts in their UV-Vis absorption spectra, confirming enhanced H-aggregation in D18 and J-aggregation in L8-BO, respectively. The optimized aggregation behavior led to higher hole and electron mobilities in the respective components, contributing to an increase in the device power conversion efficiency from 17.1% to 19.6%. This work establishes solvent-mediated aggregation control as an effective method for optimizing charge transport and improving the performance of organic solar cells.

2. Results and Discussion

Figures 1a-c illustrate the chemical structures of D18, L8-BO, EB, and CF. The UV-Vis absorption spectra of D18 film, L8-BO film, and D18:L8-BO blend film prepared using CF and mixed EB/CF solvents are shown in ESI Figures S1-2, respectively. To achieve optimal photovoltaic performance, we conducted a systematic study on the processing parameters of the D18:L8-BO system. First, we optimized the volume ratio of EB a high-boiling-point solvent additive - in the CF host solvent, adjusting it from 0% to 20% (Table S1**)**. The power conversion efficiency (PCE) first increased and then decreased with the rise in EB content, reaching a maximum value of 19.6% when the EB volume ratio was 10%. Thus, the 10% EB volume ratio was determined as the optimal formulation for all subsequent studies. We further verified the generality of this EB/CF solvent strategy in two other benchmark systems (D18:ec9-2Cl and PM6:L8-BO) (Table S2). The results showed that both systems achieved consistent performance improvements, indicating that EB has broad applicability in promoting favorable aggregation and phase separation. For comparison, we also

evaluated other common solvent additives—chlorobenzene (CB), toluene (Tol), and propylbenzene (PB)—in the D18:L8-BO system (Table S3). Although Tol (110 ℃) has a boiling point close to that of EB (136 ℃), its lower polarity resulted in less effective molecular aggregation in solution, leading to a lower PCE than that achieved with EB. In contrast, while CB exhibits higher polarity, its excessively strong polarity suppressed the necessary molecular self-assembly during film formation. Meanwhile, PB (159 ℃), with its overly high boiling point, led to excessively slow solvent evaporation, which is unfavorable for forming an ideal nanoscale phase-separated structure. Therefore, EB, with its appropriate boiling point and non-polar nature, strikes an optimal balance in promoting favorable aggregation behavior for both the donor and acceptor, thereby achieving the best performance. Finally, we optimized the thermal annealing temperature for the active layer prepared using the optimal 10% EB/CF solvent system (Table S4). Annealing at 100 ℃ resulted in the best device performance. Therefore, we adopted the 100 ℃ annealing condition as the standard procedure to stabilize the film morphology regulated by solvent engineering. The D18 donor exhibits a strong absorption band in the range of 500-600 nm. Upon addition of 10% EB, a blue shift of approximately 3 nm was observed, indicating enhanced H-aggregation of the D18 donor[27, 28]. The maximum absorption peak and the shoulder peak correspond to the 0-1 and 0-0 vibronic transitions of the π-π* electronic transition, respectively. Compared to the D18 film prepared with CF alone, the film processed with EB/CF mixed solvent showed a decreased intensity ratio of the 0-0 to 0-1 peaks, further confirming the enhancement of H-aggregation[29]. In contrast, the L8-BO acceptor exhibited a red shift of about 4 nm after the addition of EB, suggesting enhanced J-aggregation[30]. The D18:L8-BO blend film prepared with the mixed solvents demonstrated a similar trend in molecular aggregation. We further investigated the effect of thermal annealing on the UV-Vis spectra (Figure. S3–S4). The maximum absorption peak and the shoulder peak of the D18 donor correspond to the 0-1 and 0-0 vibronic transitions of the π–π* electronic transition, respectively. Compared with the as-cast D18 film, the film annealed at 100 °C shows a decreased intensity ratio of the 0-0 to 0-1 peaks, confirming enhanced H-aggregation. Meanwhile, the L8-BO acceptor

exhibits a red shift of approximately 5 nm upon EB addition after annealing, indicating enhanced J-aggregation. Similarly, the annealed D18:L8-BO blend film shows a consistent trend in molecular aggregation. Therefore, the thermal annealing treatment further optimize the molecular aggregation to improve the morphology of active layer for the device prepared by EB/CF mixed solvent. We attribute this phenomenon to the low polarity of the EB solvent, which modulates the aggregation kinetics of the D18 molecules. The weak interaction between the nonpolar ethylbenzene and the polar functional groups of the D18 donor slows the aggregation rate, thereby facilitating the formation of H-aggregation - as evidenced by the blue-shifted absorption peak and reduced coherence length observed in GIWAXS [22,27]. For L8-BO, however, the nonpolar nature of EB complements its rigid structure, promoting ordered crystallization via π-π stacking and van der Waals forces[31].

To clarify the underlying mechanism of the observed unique aggregation behavior, we employed in-situ UV-Vis absorbance spectroscopy to track the film formation processes of pure D18 and L8-BO films. As shown in Figure 1d-i, the variation of maximum absorbance with spin-coating time was extracted to verify the film formation process, where the color intensity represents the absorbance at specific times and wavelengths. Based on the in-situ UV-visible absorbance measurements (Experimental Section in SI for details), the film formation time for the neat D18 donor, determined as the time for the absorbance to reach 95% of its saturation value, was 69 ms for pure CF and 100 ms for the CF with 10% EB mixture. The time-dependent curves of maximum absorption peaks clearly indicated a blue shift upon addition of 10% EB, consistent with the aforementioned UV-Vis absorption results. Analysis of the time-resolved UV-Vis spectra during film drying and the evolution of absorption intensity within the 500-700 nm range (Figure S6) revealed that, over time, the absorption intensity at approximately 520 nm gradually increased and eventually surpassed that at around 600 nm. This suggests that the addition of EB promotes molecular H-aggregation [32, 33]. On the other hand, the pure L8-BO film formation time in pure CF and CF with 10% EB was 32 ms and 68 ms, respectively. The time-dependent maximum absorption curves showed a distinct red shift with the adhibition of 10% EB,

again consistent with previous UV-Vis findings. Analysis of time-resolved UV-Vis spectra during drying and absorption intensity evolution in the 500-1000 nm range showed the attenuated absorption peak at 850 nm with 10% EB addition.

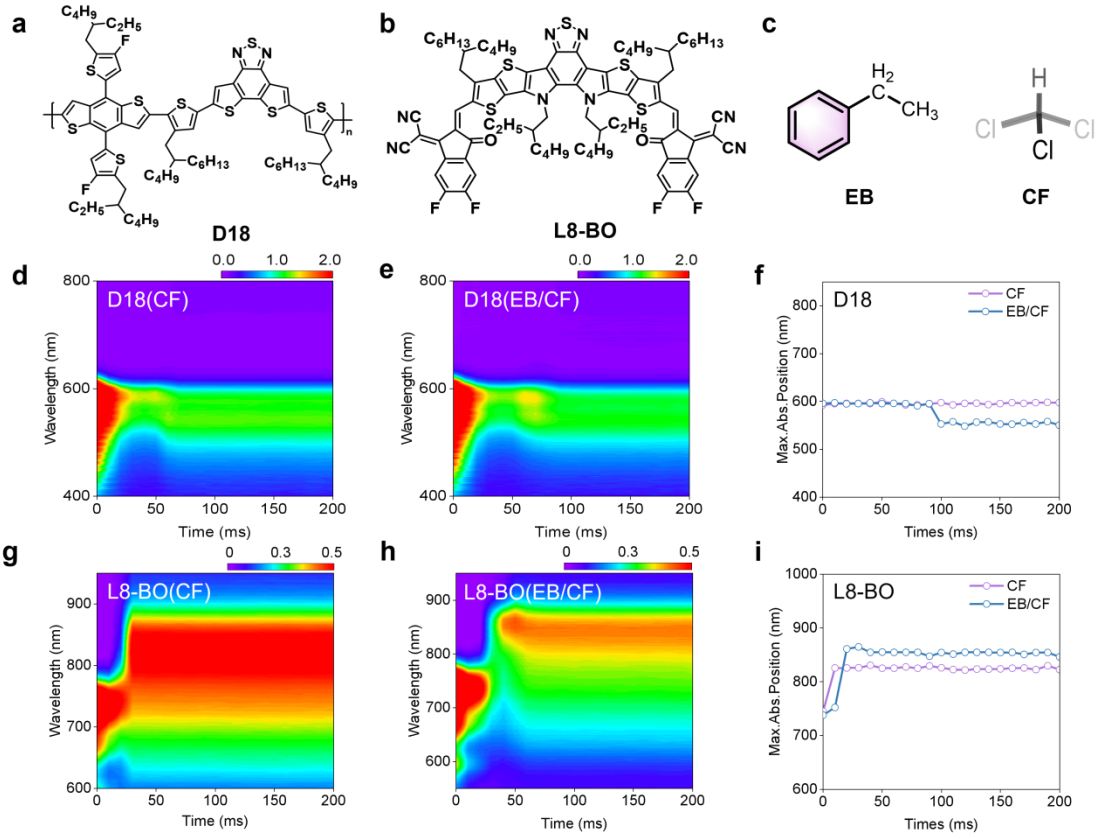

Figure 1.a) Molecular structure of D18. b) Molecular structure of L8-BO. c) Molecular structures of EB and CF. Time-dependent contour maps of in-situ UV-visible absorbance spectra of D18 during spin coating with d) CF and e) EB/CF solutions. The color scale represents the absorbance intensity. The time zero (t = 0) corresponds to the start of the spin-coating process. f) Time evolution curves of the maximum absorption wavelength of D18 in chloroform and with the addition of EB within 200 ms. Time-dependent contour maps of in-situ UV-visible absorbance spectra of L8-BO during spin coating with g) CF and h) EB/CF solutions. i) Time evolution curves of the maximum absorption wavelength of L8-BO in chloroform and with the addition of EB within 200 ms.

Subsequently, the crystallinity and molecular packing of the neat films were further probed by GIWAXS (Figure 2, Tables S5, S6). For the neat D18 film, the addition of

EB led to a significant reduction in the coherence length (CCL) of the (010) π-π stacking peak from 2.84 nm to 2.44 nm, while the π-π stacking distance remained virtually unchanged within experimental error (0.372 nm for CF and. 0.374 nm for EB/CF). This indicates that EB promotes the formation of H-aggregates with shorter-range ordered domains, which is consistent with the blue-shifted absorption and contributes to suppressing excessive crystallization of the donor. In stark contrast, for the neat L8-BO acceptor, EB treatment induced a pronounced increase in the CCL from 2.33 nm to 3.14 nm, signifying a substantial improvement in long-range molecular order and crystallinity. The concomitant slight tightening of the π-π stacking distance (from 0.360 nm to 0.357 nm) further supports this enhanced packing. These GIWAXS results unambiguously confirm that EB facilitates the formation of highly ordered J-aggregates in L8-BO, which is in full agreement with the observed red-shift in the UV-Vis spectra.

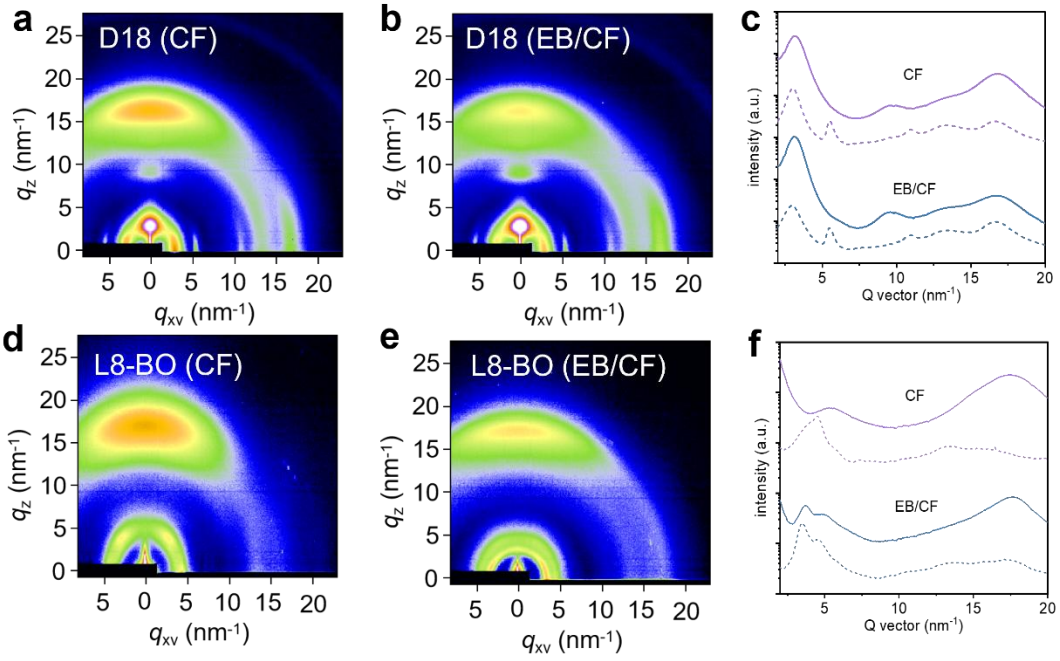

Figure 2. 2D-GIWAXS patterns of the ordered films of D18(a-b), L8-BO(d-e) without/with EB treatment. c) 1D profiles of D18 2D GIWAXS data taken along q_z (solid line) and q_{xy} (dash line) axes. d) 1D profiles of L8-BO 2D GIWAXS data taken along q_z (solid line) and q_{xy} (dash line) axes.

After analyzing the aggregation behaviors of neat D18 and L8-BO films, we further investigated the morphological evolution of the blend film treated with EB. The 2D time-resolved UV-Vis absorbance maps of the binary blend films were showed in Figure 3a-b, and accompanied by the corresponding absorption curves (Figure S8). In the D18:L8-BO blend system with 10% EB solution, the film formation time of L8-BO was prolonged owing to the higher boiling point of EB reducing solvent evaporation. Moreover, the time evolution of peak positions of L8-BO exhibited the maximum absorption peak of L8-BO underwent a significant red shift (Figure 3d), proving the enhancement of J-aggregation in the blend films[34-36]. Analysis of the time-resolved spectra further supports the modulation of molecular aggregation. For the D18 component, the spectral evolution shows a blue-shift in the absorption edge around 580-600 nm with the addition of 10% EB (Figure 3c), suggesting the enhancement of H-aggregation.[37].

The GIWAXS was used to meticulously explored the effect of EB on the crystallinity and molecular packing. The 2D GIWAXS patterns, corresponding 1D line cuts, and statistical analysis of relevant parameters for the D18:L8-BO blend film were shown in Figures 3e and S9. Detailed GIWAXS parameters were listed in Table S7. As shown in Figure 3f, the D18:L8-BO blend film exhibited a distinct (010) peak at q = 17.0 nm^{-1}, corresponding to a π-π stacking distance of 0.369 nm and a crystalline coherence length (CCL) value of 2.22 Å, indicating a preferential face-on orientation of D18:L8-BO. After the introduction of EB, the π-π stacking distance of the D18:L8-BO blend film remains essentially consistent within the experimental error range (0.369 nm for CF treatment and 0.364 nm for EB/CF treatment). However, the most notable change is that the crystalline coherence length significantly increases from 2.22 nm to 2.40 nm after EB treatment. This result demonstrates that the addition of EB can effectively enhance the aggregation ability of L8-BO and promote its crystallization. The similar and relatively isotropic orientation observed in both the neat L8-BO and the D18:L8-BO blend films suggests that the strong crystalline nature of the L8-BO acceptor dominates the packing morphology in the blend. This isotropic character, comprising a mixture of molecular orientations, is commonly observed in high-

performance NFA-based systems and is considered favorable for establishing a three-dimensional charge transport network. Based on the characterization of active layer morphology and crystallization, we speculated that the utilization of EB mitigated the excessive aggregation of D18 and promoted more compact aggregation of L8-BO via optimizing aggregation modes, respectively. The optimal aggregation behavior for donor and acceptor facilitated the hole and electron transport, respectively, thereby realizing the higher photovoltaic performance.

The active layer morphology plays an important role in the understanding of the photovoltaic performance and working mechanism, the atomic force microscopy (AFM) was used to confirm the neat D18 films and blend film based on D18:L8-BO morphology. As shown in Figures S10,11 the donor D18 exhibited decreased surface roughness (R_q) from 1.36 nm to 1.26 nm after using EB, further confirming that EB suppressed the molecular aggregation of D18. In addition, the utilization of EB increased the surface R_q of blend films from 1.42 nm to 1.98 nm, and the surface morphology transformed from fibrous to crystalline. These results indicated that the influence of EB on the molecular aggregation of active layer was L8-BO acceptor as dominance. Meanwhile, the introduction of EB facilitated more favorable aggregation modes to form ideal nanoscale phase separation, establishing the advantageous charge transport channel.

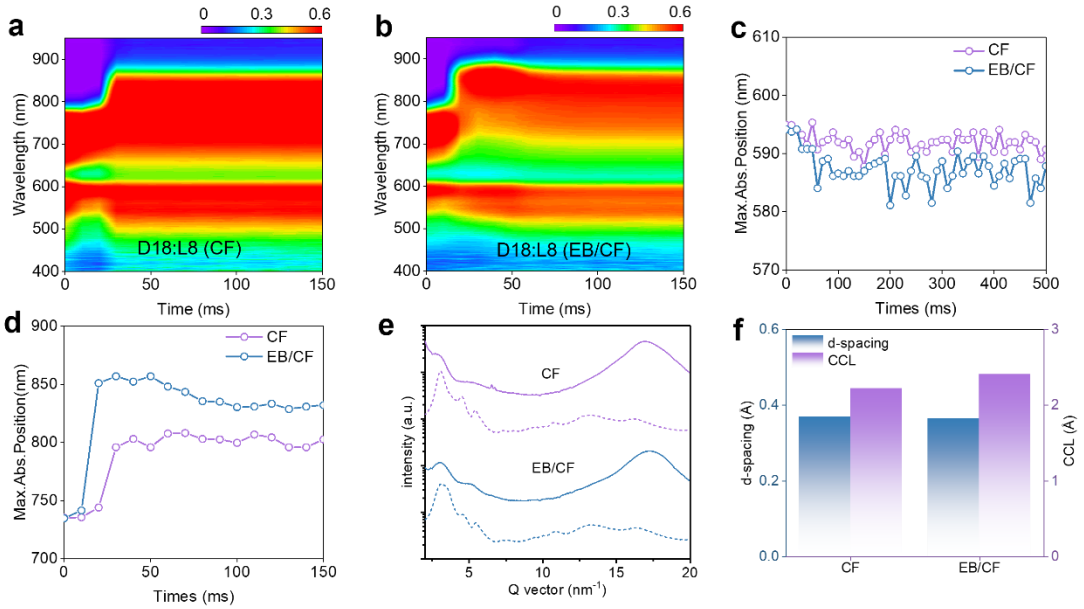

Figure 3. a- b) Time-dependent contour maps of in-situ UV-visible absorbance spectra

of D18:L8-BO blends during spin coating without/with EB treatment. The color scale represents the absorbance intensity. The time zero (t = 0) corresponds to the start of the spin-coating process. c-d) Temporal evolution of peak positions and intensities of D18 and L8-BO over time without/with EB treatment. e) 1D profiles extracted from 2D GIWAXS data of D18:L8-BO along the q_z (solid line) and q_{xy} (dashed line) axes. f) Histograms of d-spacing and CCL for blend films with and without EB treatment.

To evaluate the photovoltaic performance of devices prepared by different solvents, OSCs were fabricated on the basis of a conventional device structure of ITO/2PACZ/D18:L8-BO/PDINN/Ag. Detailed experimental conditions and optimization procedures were documented in the ESI. The current density-voltage (*J-V*) curves of the optimized ternary devices were exhibited in Figure 4a, and corresponding detailed device parameters were listed in Table 1. The OSCs prepared by pure CF yielded a PCE of 17.1%, with a J_{SC} of 25.7 mA cm^{-2}, a V_{OC} of 0.91 V, and an FF of 73.2%. When the EB was used to prepare OSCs, the device exhibited a significantly improved PCE of 19.6%, with a J_{SC} of 27.5 mA cm^{-2}, a V_{OC} of 0.90 V, and an FF of 79.0%. The statistical distributions of PCEs for the OSCs with and without EB solvent were displayed in Figure 4b. The statistical distributions of all EB-treated devices show smaller deviations, demonstrating excellent reproducibility of PCE and $J_{SC.}$ Besides, the corresponding external quantum efficiency (EQE) spectra were shown in Figure 4c. The addition of EB enhanced EQE values in the wavelength range of 550-700 nm, which contributes to the higher J_{SC}. Therefore, OSCs prepared by mixed solvents had higher J_{SC} of 26.6 mA cm^{-2} than that of OSCs prepared by pure CF (24.9 mA cm^{-2}), confirming the availability of the EB in improving the photovoltaic performance of solar cells. Furthermore, the long-term operational stability of OSCs prepared by pure CF and mixed solvents was investigated, respectively. As shown in Figure 4d, the PCE of the device without the EB degraded to ~64% of initial value after 1000 hour's light soaking stress (under 100 mW cm^{-2} white LED illumination), with a T80 lifetime (time to 80% of initial performance) of only 221 hours. In contrast, the

EB-treated device exhibited enhanced device stability under the same operating conditions, with a T80 lifetime extended to 596 hours and retention of 76% of initial PCE after 1000 hours of continuous operation. These results confirmed that the favorable donor/acceptor aggregation behavior induced by EB treatment contributed to enhanced device stability. In addition to photostability, the thermal stability of devices is another key indicator for evaluating their potential in practical applications. To investigate the effect of EB treatment on the thermal stability of the active layer, we conducted thermal stability tests. Figure S18 shows the normalized efficiency decay curves of the devices under a nitrogen atmosphere at a constant temperature of 60 °C. For the devices treated with pure CF, their efficiency dropped to 80% of the initial value within 300 hours. In contrast, the devices treated with the EB/CF mixed solvent exhibited a slower decay, with the T80 lifetime extended to 400 hours. This enhanced thermal stability can be attributed to the more stable active layer morphology induced by EB. Together with the photostability test results, these findings indicate that our solvent engineering strategy can simultaneously improve the photostability and thermal stability of the devices, laying a more solid foundation for their practical applications. To investigate exciton dissociation and charge collection behavior in the devices, we measured the dependence of photocurrent density (J_{ph}) on effective voltage (V_{eff}). Under short-circuit conditions, the exciton dissociation probability (P_{diss}) can be estimated by the ratio of J_{ph}/J_{sat}, while the charge collection probability (P_{coll}) can be similarly evaluated at the maximum power output point using an analogous approach. Figure S19 show that the EB/CF-processed device exhibits superior exciton dissociation efficiency, with a P_{diss} of 97.66%, higher than the 95.44% of the CF-processed device, indicating more efficient exciton dissociation. Furthermore, to study the charge recombination mechanisms in the devices, we analyzed the variation of open-circuit voltage (V_{OC}) with light intensity (P_{light}). The relationship between V_{OC} and light intensity (P_{light}) provides insight into recombination behavior, where the slope of V_{OC} versus $\ln(P_{light})$, when normalized by k_BT/q (k_B: Boltzmann constant, T: temperature, q: elementary charge), yields the recombination parameter β. A β value close to 1 signifies dominant bimolecular recombination, while a value near 2 indicates strong monomolecular

recombination[38-40]. As shown in Figure S12, the device processed with pure CF exhibits a β value of 1.409, whereas the mixed-solvent system shows a reduced β of 1.205. These results indicating that bimolecular recombination is the main loss mechanism in both systems, and the mixed-solvent system effectively suppresses charge recombination. In summary, the EB/CF processing not only improves exciton dissociation and charge collection efficiency but also reduces charge recombination losses.

Transient absorption spectroscopy (TAS) was employed to investigate the carrier dynamics within the active layer and establish connections among film morphology, exciton dissociation, and charge transport[41, 42]. Based on the normalized UV–vis absorption spectra of the donor and acceptor, an excitation wavelength of 800 nm was selected to selectively excite the L8-BO acceptor in the blend film, enabling clear observation of hole transfer from L8-BO to D18. The TAS spectra of films processed with pure CF and with 10% EB additive are presented in Figure S13. Following excitation, both blend films exhibit a pronounced ground-state bleaching (GSB) signal in the long-wavelength region (560–830 nm), accompanied by a gradually intensifying negative signal in the short-wavelength region (510–620 nm). These spectral features are attributed to exciton generation in L8-BO and the evolving hole transfer process, respectively.

To quantitatively evaluate the hole transfer dynamics, kinetic traces at representative wavelengths were extracted. As illustrated in the time-delayed TA spectra (Figure S14), the GSB signal of L8-BO at 810 nm decays markedly, while that of D18 at 594 nm rises simultaneously, indicating efficient hole transfer from L8-BO to D18. The rise dynamics of the D18 GSB signal directly reflect the hole transfer kinetics. We applied a bi-exponential fitting model to analyze the rising component of the D18 GSB signal at 594 nm, extracting two characteristic time constants: τ_1, representing the ultrafast exciton dissociation at the donor/acceptor (D/A) interface, and τ_2, corresponding to the total duration for exciton diffusion from the acceptor phase to the D/A interface followed by dissociation. The results are summarized in Figures S15 and S16.

For the D18:L8-BO system processed with pure CF, τ_1 = 0.46 ps and τ_2 = 12.5 ps, whereas for the system with 10% EB additive, τ_1 = 0.36 ps and τ_2 = 10.6 ps. The shorter τ_1 and τ_2 values in the EB-added system indicate accelerated exciton dissociation and reduced overall hole transfer time, suggesting that EB promotes more efficient interfacial charge separation. The decrease in τ_2 indicates accelerated exciton dissociation and a reduced overall hole transfer time in the EB-processed system. This suggests that utilization of EB optimized molecular aggregation behavior to promote more efficient interfacial charge separation, which aligns with the optimized nanoscale morphology achieved through solvent engineering.

Considering the influence of donor and acceptor molecular aggregation modes on charge transport, we employed the space-charge-limited current (SCLC) method to measure the charge carrier mobilities of blend films fabricated using pure CF and mixed EB/CF solvents[43, 44]. The relevant parameters are summarized in Figure S17 and Table S8. The test results demonstrate that the use of EB optimized the aggregation behavior of both D18 and L8-BO in the blend films. As a result, compared to the blend film prepared with pure CF (with $\mu_h = 1.53\times10^{-4}$ cm^2 V^{-1} s^{-1} and $\mu_e = 1.01\times10^{-4}$ cm^2 V^{-1} s^{-1}), the hole and electron mobilities were significantly enhanced to 3.60×10^{-4} cm^2 V$^{-1}\cdot$s^{-1} and 3.07×10^{-4} cm^2 V$^{-1}\cdot$s^{-1}, respectively. Notably, the EB-treated blend film exhibited a more balanced hole/electron mobility ratio (≈1.17) compared to that of the pure CF-based blend film (≈1.51). Consequently, devices fabricated with the mixed EB/CF solvent achieved a higher FF.

To gain deeper insight into the charge transport and collection processes within the devices, transient photocurrent (TPC) measurement was performed on the organic active layer films[45]. As shown in Figure 4e, the charge extraction time (τ) under operating conditions was determined through nonlinear fitting of the current-time and voltage-time curves. Compared to the device fabricated with pure CF, the device prepared with mixed solvents exhibited a shorter charge extraction time (decreased from 0.486 μs to 0.362 μs). These results indicate that the incorporation of EB effectively enhances charge carrier collection and suppresses charge recombination, leading to an improved J_{SC} in the OSCs.

Further investigation into the impact of trap state density (N_t) on device performance was carried out using deep-level transient spectroscopy (DLTS)[46]. A rapid increase in N_t is a critical factor contributing to the performance degradation of OSCs. DLTS characterization revealed that the device prepared with mixed solvents had a lower N_t of 3.63×10^{15} cm^{-3}, compared to 4.11×10^{15} cm^{-3} for the pure CF-based device (Figure 4f). Therefore, the addition of EB effectively reduces the trap state density in the device and slows molecular diffusion within the blend system, thereby contributing to superior J_{SC} and FF.

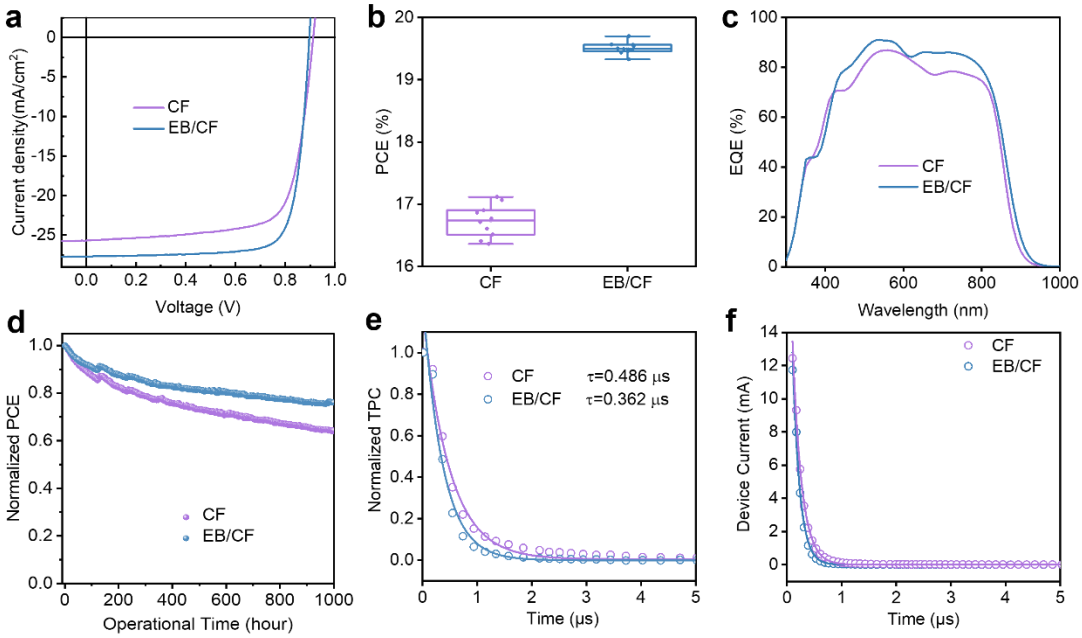

Figure 4. a) The *J-V* curves of neat CF and EB/CF mixed solvent treated devices. b) The statistical PCE of neat CF and EB/CF mixed solvent treated devices. c) EQE spectra of neat CF and EB/CF mixed solvent treated devices. d) The long-term photostability of neat CF and EB/CF mixed solvent treated devices. e) The TPC curves of neat CF and EB/CF mixed solvent treated devices. f) The DLTS curves of t of neat CF and EB/CF mixed solvent treated devices.

Table 1. The photovoltaic performance of D18:L8-BO without and with EB treatment by 10 separate devices.

Solvent	V_{OC} [V]	J_{SC} [mA/cm^{-2}]	J_{SC}^{EQE} [mA/cm^{-2}]	FF [%]	PCE [%]
CF	0.91	25.7	24.9	73.2	17.1
	(0.90±0.01)	(24.2±2.5)		(70.1±3.0)	(16.8±0.3)
EB/CF	0.90	27.5	26.6	79.0	19.6
	(0.89±0.01)	(26.1±1.7)		(76.1±3.0)	(19.3±0.3)

In conclusion, it was found that aggregation modes of D18 donor and L8-BO acceptor could be tuned by using the mixed solvents of EB and CF. The utilization of EB could induce the more H- and J-aggregation for D18 donor and L8-BO acceptor, which facilitated the hole and electron transport in the active layer, respectively. Moreover, the optimal aggregation modes of D18 donor and L8-BO acceptor conduced to forming ideal nanoscale phase separation, which effectively hindered bimolecular recombination to improve charge transfer. Therefore, the OSCs prepared by mixed EB/CF realized an impressive PCE of 19.6% with an enhanced J_{SC} of 27.5 mA cm^{-2} and a higher FF of 79.0%. Furthermore, the optimal device exhibits simultaneously enhanced photostability and thermal stability. Under continuous light illumination, its T80 lifetime is extended from 221 hours to 596 hours; under thermal aging conditions at 60 ℃, its T80 lifetime is also prolonged from 300 hours to 400 hours. Hence, this work provides a reliable strategy to optimize aggregation modes of donor and acceptor, which contribute to improving the photovoltaic performance of OSCs in a targeted way.

Acknowledgements

This work was financially supported by National Natural Science Foundation of China (22575029, 62105129). The authors also thank National Synchrotron Light Source II (NSLS-II, Contract No. DE- SC0012704) Brookhaven National Laboratory for providing GIWAXS experiment time.

REFERENCES

[1] M. Dong, S. Chen, L. Hong, J. Jing, Y. Bai, Y. Liang, C. Zhu, T. Shi, W. Zhong, L. Ying, K. Zhang, F. Huang, 19.0% efficiency binary organic solar cells enabled by using a building block as solid additive, Nano Energy 119 (2024) 109097. https://doi.org/https://doi.org/10.1016/j.nanoen.2023.109097.
[2] Y. Liu, B. Liu, C.-Q. Ma, F. Huang, G. Feng, H. Chen, J. Hou, L. Yan, Q. Wei, Q. Luo, Q. Bao, W. Ma, W. Liu, W. Li, X. Wan, X. Hu, Y. Han, Y. Li, Y. Zhou, Y. Zou, Y. Chen, Y. Li, Y. Chen, Z. Tang, Z. Hu, Z.-G. Zhang, Z. Bo, Recent progress in organic solar cells (Part I material science), Sci. China Chem. 65(2) (2022) 224-268. https://doi.org/10.1007/s11426-021-1180-6.
[3] J. Yuan, Y. Zhang, L. Zhou, G. Zhang, H.-L. Yip, T.-K. Lau, X. Lu, C. Zhu, H. Peng, P.A. Johnson, M. Leclerc, Y. Cao, J. Ulanski, Y. Li, Y. Zou, Single-Junction Organic Solar Cell with over 15% Efficiency Using Fused-Ring Acceptor with Electron-Deficient Core, Joule 3(4) (2019) 1140-1151. https://doi.org/https://doi.org/10.1016/j.joule.2019.01.004.
[4] Y. Cho, Z. Sun, G. Li, D. Zhang, S. Yang, T.J. Marks, C. Yang, A. Facchetti, CF3-Functionalized Side Chains in Nonfullerene Acceptors Promote Electrostatic Interactions for Highly Efficient Organic Solar Cells, J. Am. Chem. Soc. 147(1) (2025) 758-769. https://doi.org/10.1021/jacs.4c13471.
[5] K. Wang, J. Liang, Z. Li, H. Zhou, C. Nie, J. Deng, X. Zhao, X. Peng, Z. Chen, Z. Peng, D. Huang, H.S. Jang, J. Kong, Y. Zou, Design of experiments with the support of machine learning for process parameter optimization of all-small-molecule organic solar cells, FlexMat 1(3) (2024) 234-247. https://doi.org/https://doi.org/10.1002/flm2.34.
[6] L. Zhang, Z. Zhuo, X. Ma, H. Tian, X. Zhao, Y. Xie, K. Yang, B.H. Lee, X. Zhu, H.Y. Woo, C. Yang, X. Nie, F. Zhang, 19.6% efficiency of layer-by-layer organic photovoltaics with decreased energy loss via incorporating TADF materials with intrinsic reverse intersystem crossing, Energ. Environ. Sci. 18(20) (2025) 9171-9182. https://doi.org/10.1039/D5EE03118D.
[7] W. Xu, H. Zhou, H. Tian, L. Zhang, J. Du, J. Yao, S.Y. Jeong, H.Y. Woo, E. Zhou, X. Ma, F. Zhang, Achieving light utilization efficiency of 3.88% and efficiency of 14.04% for semitransparent layer-by-layer organic solar cells by diluting donor layer, Chem. Eng. J. 508 (2025) 161148. https://doi.org/https://doi.org/10.1016/j.cej.2025.161148.
[8] H. Zhou, L. Zhang, H. Tian, Y. Ni, Y. Xie, S.Y. Jeong, T. Huang, H.Y. Woo, J. Zhang, X. Zhu, L. Lu, X. Ma, F. Zhang, Layered All-Polymer Solar Cells with Efficiency of 18.34% by Employing Alloyed Polymer Donors, Small 21(11) (2025) 2410581. https://doi.org/https://doi.org/10.1002/smll.202410581.
[9] Q. Wei, W. Liu, M. Leclerc, J. Yuan, H. Chen, Y. Zou, A-DA′D-A non-fullerene acceptors for high-performance organic solar cells, Sci. China Chem. 63(10) (2020) 1352-1366. https://doi.org/10.1007/s11426-020-9799-4.
[10] L. Zhan, S. Li, Y. Li, R. Sun, J. Min, Z. Bi, W. Ma, Z. Chen, G. Zhou, H. Zhu, M. Shi, L. Zuo, H. Chen, Desired open-circuit voltage increase enables efficiencies approaching 19% in symmetric-asymmetric molecule ternary organic photovoltaics, Joule 6(3) (2022) 662-675. https://doi.org/https://doi.org/10.1016/j.joule.2022.02.001.
[11] Y. Dong, H. Cha, H.L. Bristow, J. Lee, A. Kumar, P.S. Tuladhar, I. McCulloch, A.A. Bakulin, J.R. Durrant, Correlating Charge-Transfer State Lifetimes with Material Energetics in Polymer:Non-Fullerene Acceptor Organic Solar Cells, J. Am. Chem. Soc. 143(20) (2021) 7599-7603. https://doi.org/10.1021/jacs.1c00584.
[12] J.W. Jo, J.W. Jung, H.-W. Wang, P. Kim, T.P. Russell, W.H. Jo, Fluorination of Polythiophene Derivatives for High Performance Organic Photovoltaics, Chem. Mater. 26(14) (2014) 4214-4220. https://doi.org/10.1021/cm502229k.
[13] R. Ma, H. Li, T.A. Dela Peña, H. Wang, C. Yan, P. Cheng, J. Wu, G. Li, In-situ understanding on the

formation of fibrillar morphology in green solvent processed all-polymer solar cells, Natl. Sci. Rev. 11(12) (2024) nwae384. https://doi.org/10.1093/nsr/nwae384.
[14] Y. Sun, L. Wang, C. Guo, J. Xiao, C. Liu, C. Chen, W. Xia, Z. Gan, J. Cheng, J. Zhou, Z. Chen, J. Zhou, D. Liu, T. Wang, W. Li, π-Extended Nonfullerene Acceptor for Compressed Molecular Packing in Organic Solar Cells To Achieve over 20% Efficiency, J. Am. Chem. Soc. 146(17) (2024) 12011-12019. https://doi.org/10.1021/jacs.4c01503.
[15] J.A. Bartelt, J.D. Douglas, W.R. Mateker, A.E. Labban, C.J. Tassone, M.F. Toney, J.M.J. Fréchet, P.M. Beaujuge, M.D. McGehee, Controlling Solution-Phase Polymer Aggregation with Molecular Weight and Solvent Additives to Optimize Polymer-Fullerene Bulk Heterojunction Solar Cells, Adv. Energy Mater. 4(9) (2014) 1301733. https://doi.org/https://doi.org/10.1002/aenm.201301733.
[16] W. Feng, Y. Bai, J. Wang, Y. Zhong, J. Wang, T. Chen, J. Zhang, K. Han, X. Wan, B. Kan, Y. Chen, Rational Design of Two Well-Compatible Dimeric Acceptors Through Regulating Chalcogen-Substituted Conjugated Backbone Enable Ternary Organic Solar Cells with 19.4% Efficiency, Adv. Energy Mater. n/a(n/a) (2024) 2404062. https://doi.org/https://doi.org/10.1002/aenm.202404062.
[17] S. Lilliu, T. Agostinelli, E. Pires, M. Hampton, J. Nelson, J.E. Macdonald, Dynamics of Crystallization and Disorder during Annealing of P3HT/PCBM Bulk Heterojunctions, Macromolecules 44(8) (2011) 2725-2734. https://doi.org/10.1021/ma102817z.
[18] F. Qi, H. Zhang, S. Liu, Y. Wei, H. Lu, G. Ran, P. Zhang, H. Li, W. Zhang, Y. Liu, Z. Bo, A Dimer Acceptor with Intramolecular Non-Covalent Interactions for Low Energy Loss, Highly Efficient and Stable Organic Solar Cells, Adv. Funct. Mater. n/a(n/a) (2025) 2424978. https://doi.org/https://doi.org/10.1002/adfm.202424978.
[19] Y. Shi, J. Pan, J. Yu, J. Zhang, F. Gao, K. Lu, Z. Wei, Optimizing the Charge Carrier and Light Management of Nonfullerene Acceptors for Efficient Organic Solar Cells with Small Nonradiative Energy Losses, Sol. Rrl 5(4) (2021) 2100008. https://doi.org/https://doi.org/10.1002/solr.202100008.
[20] X. Zheng, Y. Wang, T. Chen, Y. Kong, X. Wu, C. Zhou, Q. Luo, C.-Q. Ma, L. Zuo, M. Shi, H. Chen, Realizing record efficiencies for ultra-thin organic photovoltaics through step-by-step optimizations of silver nanowire transparent electrodes, FlexMat 1(3) (2024) 221-233. https://doi.org/https://doi.org/10.1002/flm2.30.
[21] G. Liu, J. Jia, K. Zhang, X.e. Jia, Q. Yin, W. Zhong, L. Li, F. Huang, Y. Cao, 15% Efficiency Tandem Organic Solar Cell Based on a Novel Highly Efficient Wide-Bandgap Nonfullerene Acceptor with Low Energy Loss, Adv. Energy Mater. 9(11) (2019) 1803657. https://doi.org/https://doi.org/10.1002/aenm.201803657.
[22] C. McDowell, M. Abdelsamie, M.F. Toney, G.C. Bazan, Solvent Additives: Key Morphology-Directing Agents for Solution-Processed Organic Solar Cells, Adv. Mater. 30(33) (2018) 1707114. https://doi.org/https://doi.org/10.1002/adma.201707114.
[23] J. Song, C. Zhang, C. Li, J. Qiao, J. Yu, J. Gao, X. Wang, X. Hao, Z. Tang, G. Lu, R. Yang, H. Yan, Y. Sun, Non-halogenated Solvent-Processed Organic Solar Cells with Approaching 20 % Efficiency and Improved Photostability, Angew. Chem. Int. Edit. 63(22) (2024) e202404297. https://doi.org/https://doi.org/10.1002/anie.202404297.
[24] Z. Tu, M.J. Zachman, S. Choudhury, S. Wei, L. Ma, Y. Yang, L.F. Kourkoutis, L.A. Archer, Rechargeable Batteries: Nanoporous Hybrid Electrolytes for High-Energy Batteries Based on Reactive Metal Anodes (Adv. Energy Mater. 8/2017), Adv. Energy Mater. 7(8) (2017). https://doi.org/https://doi.org/10.1002/aenm.201770039.
[25] J. Wu, Z. Ling, L.R. Franco, S.Y. Jeong, Z. Genene, J. Mena, S. Chen, C. Chen, C.M. Araujo, C.F.N.

Marchiori, J. Kimpel, X. Chang, F.H. Isikgor, Q. Chen, H. Faber, Y. Han, F. Laquai, M. Zhang, H.Y. Woo, D. Yu, T.D. Anthopoulos, E. Wang, On the Conformation of Dimeric Acceptors and Their Polymer Solar Cells with Efficiency over 18 %, Angew. Chem. Int. Edit. 62(45) (2023) e202302888. https://doi.org/https://doi.org/10.1002/anie.202302888.

[26] B. Yang, B. Cai, T. Zhou, X. Zheng, W.-H. Zhang, Facile and sustainable interface modulation via a self-assembly phosphonate molecule for efficient and stable perovskite photovoltaics, Chem. Eng. J. 488 (2024) 150861. https://doi.org/https://doi.org/10.1016/j.cej.2024.150861.

[27] H. Hu, M. Ghasemi, Z. Peng, J. Zhang, J.J. Rech, W. You, H. Yan, H. Ade, The Role of Demixing and Crystallization Kinetics on the Stability of Non-Fullerene Organic Solar Cells, Adv. Mater. 32(49) (2020) 2005348. https://doi.org/https://doi.org/10.1002/adma.202005348.

[28] H. Lu, W. Liu, G. Ran, J. Li, D. Li, Y. Liu, X. Xu, W. Zhang, Z. Bo, High-Efficiency Binary and Ternary Organic Solar Cells Based on Novel Nonfused-Ring Electron Acceptors, Adv. Mater. 36(7) (2024) 2307292. https://doi.org/https://doi.org/10.1002/adma.202307292.

[29] X. Song, L. Mei, X. Zhou, H. Li, H. Xu, X. Liu, S. Gao, S. Xu, Y. Yang, W. Zhu, J. Wang, X.-H. Zhang, X.-K. Chen, Frenkel and Charge-Transfer Excitonic Couplings Strengthened by Thiophene-Type Solvent Enables Binary Organic Solar Cells with 19.8 % Efficiency, Angew. Chem. Int. Edit. 63(44) (2024) e202411512. https://doi.org/https://doi.org/10.1002/anie.202411512.

[30] S. Shi, P. Chen, Y. Chen, K. Feng, B. Liu, J. Chen, Q. Liao, B. Tu, J. Luo, M. Su, H. Guo, M.-G. Kim, A. Facchetti, X. Guo, A Narrow-Bandgap n-Type Polymer Semiconductor Enabling Efficient All-Polymer Solar Cells, Adv. Mater. 31(46) (2019) 1905161. https://doi.org/https://doi.org/10.1002/adma.201905161.

[31] J. Wang, Y. Wang, P. Bi, Z. Chen, J. Qiao, J. Li, W. Wang, Z. Zheng, S. Zhang, X. Hao, J. Hou, Binary Organic Solar Cells with 19.2% Efficiency Enabled by Solid Additive, Adv. Mater. 35(25) (2023) 2301583. https://doi.org/https://doi.org/10.1002/adma.202301583.

[32] M. Du, Y. Chen, M. Mai, T. Fan, Q. Jin, Y. Zhang, L. Duan, Understanding and modulating the horizontal orientations and short-range charge transfer excited states for high-performance narrowband emitters, FlexMat 1(1) (2024) 46-53. https://doi.org/https://doi.org/10.1002/flm2.15.

[33] L. Guo, J. Song, J. Deng, J. Qiao, J. Zhang, C. Li, S. Yuan, B. Han, M.H. Jee, Z. Ge, C. Zhang, G. Lu, X. Hao, H.Y. Woo, Y. Sun, Suppression of Charge Recombination Induced by Solid Additive Assisting Organic Solar Cells with Efficiency over 20%, Adv. Mater. 37(24) (2025) 2504396. https://doi.org/https://doi.org/10.1002/adma.202504396.

[34] Y. Li, F. Qi, B. Fan, K.-K. Liu, J. Yu, Y. Fu, X. Liu, Z. Wang, S. Zhang, G. Lu, X. Lu, Q. Fan, P.C.Y. Chow, W. Ma, F.R. Lin, A.K.Y. Jen, Eliminating the Burn-in Loss of Efficiency in Organic Solar Cells by Applying Dimer Acceptors as Supramolecular Stabilizers, Adv. Mater. 36(23) (2024) 2313393. https://doi.org/https://doi.org/10.1002/adma.202313393.

[35] C. Liao, X. Xu, T. Yang, W. Qiu, Y. Duan, R. Li, L. Yu, Q. Peng, Tetrahydrofuran Processable Organic Solar Cells with 19.45% Efficiency Realized by Introducing High Molecular Dipole Unit Into the Terpolymer, Adv. Mater. 36(48) (2024) 2411071. https://doi.org/https://doi.org/10.1002/adma.202411071.

[36] X. Luo, J. Yu, H. Tang, H. Cai, W. Xiong, K. Zhang, F. Huang, Y. Cao, Self-doped conjugated polymers with electron-deficient quinone units for enhanced electron transport in highly efficient organic solar cells, FlexMat 1(2) (2024) 105-115. https://doi.org/https://doi.org/10.1002/flm2.17.

[37] X. Zhang, J. Cai, C. Guo, D. Li, B. Du, Y. Zhuang, S. Cheng, L. Wang, D. Liu, T. Wang, Simultaneously Enhanced Efficiency and Operational Stability of Nonfullerene Organic Solar Cells via

Solid-Additive-Mediated Aggregation Control, Small 17(35) (2021) 2102558. https://doi.org/https://doi.org/10.1002/smll.202102558.
[38] L. Chen, C. Zhao, H. Yu, A. Sergeev, L. Zhu, K. Ding, Y. Fu, H.M. Ng, C.H. Kwok, X. Zou, J. Yi, X. Lu, K.S. Wong, H. Ade, G. Zhang, H. Yan, Tailoring Cyano Substitutions on Quinoxaline-based Small-Molecule Acceptors Enabling Enhanced Molecular Packing for High-Performance Organic Solar Cells, Adv. Energy Mater. 14(30) (2024) 2400285. https://doi.org/https://doi.org/10.1002/aenm.202400285.
[39] S.R. Cowan, A. Roy, A.J. Heeger, Recombination in polymer-fullerene bulk heterojunction solar cells, Phys. Rev. B 82(24) (2010) 245207. https://doi.org/10.1103/PhysRevB.82.245207.
[40] J. Fu, H. Chen, P. Huang, Q. Yu, H. Tang, S. Chen, S. Jung, K. Sun, C. Yang, S. Lu, Z. Kan, Z. Xiao, G. Li, Eutectic phase behavior induced by a simple additive contributes to efficient organic solar cells, Nano Energy 84 (2021) 105862. https://doi.org/https://doi.org/10.1016/j.nanoen.2021.105862.
[41] L. Kong, Z. Zhang, N. Zhao, Z. Cai, J. Zhang, M. Luo, X. Wang, M. Chen, W. Zhang, L. Zhang, Z. Wei, J. Chen, In Situ Removable Additive Assisted Organic Solar Cells Achieving Efficiency over 19% and Fill Factor Exceeding 81%, Adv. Energy Mater. 13(25) (2023) 2300763. https://doi.org/https://doi.org/10.1002/aenm.202300763.
[42] Z. Sun, H. Ma, S. Yang, Y. Cho, S. Lee, J. Park, T.L.H. Mai, W. Kim, S. Jeong, S. Kim, C. Yang, Insight Into Designing High-Performance Polythiophenes for Reduced Urbach Energy and Nonradiative Recombination in Organic Solar Cells, Adv. Funct. Mater. 34(39) (2024) 2403093. https://doi.org/https://doi.org/10.1002/adfm.202403093.
[43] W. Liang, L. Chen, Z. Wang, Z. Peng, L. Zhu, C.H. Kwok, H. Yu, W. Xiong, T. Li, Z. Zhang, Y. Wang, Y. Liao, G. Zhang, H. Hu, Y. Chen, Oligothiophene Additive-Assisted Morphology Control and Recombination Suppression Enable High-Performance Organic Solar Cells, Adv. Energy Mater. 14(11) (2024) 2303661. https://doi.org/https://doi.org/10.1002/aenm.202303661.
[44] D.B. Riley, O.J. Sandberg, N. Zarrabi, Y.R. Kim, P. Meredith, A. Armin, Efficient Nanoscale Exciton Transport in Non-Fullerene Organic Solar Cells Enables Reduced Bimolecular Recombination of Free Charges, Adv. Mater. 35(24) (2023) 2211174. https://doi.org/https://doi.org/10.1002/adma.202211174.
[45] T. Zhou, W. Jin, Y. Li, X. Xu, Y. Duan, R. Li, L. Yu, Q. Peng, Crossbreeding Effect of Chalcogenation and Iodination on Benzene Additives Enables Optimized Morphology and 19.68% Efficiency of Organic Solar Cells, Adv. Mater. 11(23) (2024) 2401405. https://doi.org/https://doi.org/10.1002/advs.202401405.
[46] Y. Zhu, D. He, C. Wang, X. Han, Z. Liu, K. Wang, J. Zhang, X. Shen, J. Li, Y. Lin, C. Wang, Y. He, F. Zhao, Suppressing Exciton-Vibration Coupling to Prolong Exciton Lifetime of Nonfullerene Acceptors Enables High-Efficiency Organic Solar Cells, Angew. Chem. Int. Edit. 63(8) (2024) e202316227. https://doi.org/https://doi.org/10.1002/anie.202316227.